



HAL
open science

Adaptation of the virtual fields method for the identification of biphasic hyperelastic model parameters in soft biological tissues with osmotic swelling

Ruike Shi, Stéphane Avril, Haitian Yang, Víctor Acosta Santamaría, Yue Mei, Yiqian He

► To cite this version:

Ruike Shi, Stéphane Avril, Haitian Yang, Víctor Acosta Santamaría, Yue Mei, et al.. Adaptation of the virtual fields method for the identification of biphasic hyperelastic model parameters in soft biological tissues with osmotic swelling. *Strain*, In press, 10.1111/str.12435 . hal-04035036

HAL Id: hal-04035036

<https://cnrs.hal.science/hal-04035036>

Submitted on 17 Mar 2023

HAL is a multi-disciplinary open access archive for the deposit and dissemination of scientific research documents, whether they are published or not. The documents may come from teaching and research institutions in France or abroad, or from public or private research centers.

L'archive ouverte pluridisciplinaire **HAL**, est destinée au dépôt et à la diffusion de documents scientifiques de niveau recherche, publiés ou non, émanant des établissements d'enseignement et de recherche français ou étrangers, des laboratoires publics ou privés.

21 The biphasic hyperelastic constitutive models of hydrated biological tissues were origi-
22 nally introduced by Eringen and Ingram in the 1960s^[5, 6]. These biphasic models have been
23 widely used in the biomechanics research of soft biological tissues. For instance,

24 — In the field of the biomechanics of cartilage, Mow et al.^[7] and Lai et al.^[8] estab-
25 lished a biphasic model and a triphasic model. These models include mainly the collagen-
26 proteoglycan matrix and the interstitial fluid, respectively. Then Ateshian et al.^[9–11] applied
27 for the models to articular cartilage with osmotic loading. Besides, Wilson et al.^[12] studied
28 the links between the biphasic swelling theories and mechano-electrochemical models. Wayne
29 et al.^[13] developed a u - p finite element model for biphasic theory by coupling deformation and
30 fluid pressure. Recently, Kandil et al.^[14] proposed a microstructure-based chemo-viscoelastic
31 model considering the osmo-induced deformation and internal fluid variation.

32 — In the field of biomechanics of arteries, Lanir^[1, 4] developed the biocomponent theory
33 in 1987. He applied this theory to residual stresses of cardiovascular tissues. Then Azeloglu
34 et al.^[15] proposed a numerical model combining the triphasic theory of Lai et al.^[8] with
35 the FEM to study the influence of proteoglycans on residual stresses in the aorta. Their
36 model was eventually validated experimentally. Recently Santamaría et al.^[16, 17] developed
37 experimental methods for quantifying the chemoelastic effects in arterial tissues.

38 All those studies showed the importance of biphasic or triphasic theory to investigate the
39 biomechanics of hydrated biological tissues, such as cartilage and arteries.

40 The identification of constitutive model parameters for soft biological tissues is still
41 flourishing^[18, 19]. Among the available identification approaches, the virtual fields method
42 (VFM) has been widely used in solid mechanics^[20–26], given its advantages, such as its insen-
43 sitivity to the uncertainty of boundary conditions^[27], robustness^[28], and fast convergence^[29].
44 Avril et al.^[30] first applied VFM to arterial tissues to identify anisotropic hyperelastic ma-
45 terial parameters. Kim et al.^[31] used VFM to identify the material properties of human
46 aneurysmal aortas. Bersi et al.^[32] collected full-field biaxial data and used the VFM to
47 estimate regional variations in material parameters for a microstructurally motivated con-
48 stitutive model.

49 The identification of biphasic hyperelastic model parameters has been rather challenging.
50 Nadeen et al.^[33] designed an apparatus for measuring osmotic pressure and estimated how
51 it contributes to cartilage stiffness. More recently, Santamaría et al.^[17] measured 3D strain
52 fields induced by chemoelastic effects in arteries. These studies showed the significance of
53 the biphasic constitutive model in arteries. Nevertheless, to the best of the authors' knowl-
54 edge, there has been no existing work dedicated to the identification of biphasic constitutive
55 models using VFM. Besides, although soft tissues (e.g. arterial wall) could be multi-layered
56 structures, there is no work on the identification of layer-specific parameters for soft tissues
57 in the framework of biphasic hyperelastic model.

58 The objective of this work is to address this lack. Considering that biphasic constitu-
59 tive models are computationally challenging due to coupling between elasticity and osmotic
60 effects, we designed a novel specific VFM framework for chemoelasticity.

61 The paper is organized as follows: Section 2 introduces the materials and methods,
62 including constitutive relationship for biphasic hyperelasticity, general principle for VFM

63 and the application of VFM for biphasic hyperelasticity. Section 3 reports the results of the
 64 verification of the proposed model and its application into practical problems, first conducted
 65 with simulated data and then with experimental data. Finally, the conclusion and discussion
 66 are given in Section 4.

67 2. Materials and methods

68 2.1. The introduction for biphasic hyperelasticity in arterial tissues

69 The framework of the biphasic constitutive relationship used in this paper is proposed
 70 by Azeloglu et al.^[15], in which the residual stresses are hypothesized to arise from the fixed-
 71 charge density of the proteoglycans present in the arterial tissues, inducing the Donnan
 72 osmotic pressure relative to the external environment as only equilibrium conditions are
 73 considered for simplicity, when the solid and fluid velocities have reduced to zero. Therefore,
 74 the Cauchy stress \mathbf{T} is assumed to have two components:

$$\mathbf{T} = \mathbf{T}_i + \mathbf{T}_s \quad (1)$$

75 where \mathbf{T}_i is the interstitial fluid component and \mathbf{T}_s is the solid matrix component.

76 As illustrated in Fig. 1, the total deformation gradient \mathbf{F} is realized by the multiplying a
 77 prestretched part \mathbf{F}_{pre} and a mechanical part \mathbf{F}_m ^[14]. The \mathbf{F}_{pre} is a stress-free swelling due to
 osmotic effects without any mechanical loading. Therefore, the total deformation gradient

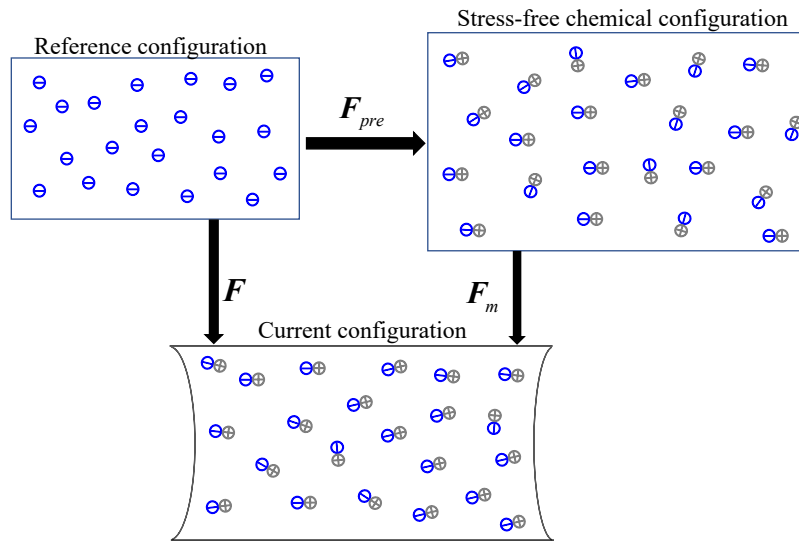


Figure 1: Multiplicative decomposition of the deformation gradient \mathbf{F}

78 \mathbf{F} can be decomposed into two parts
 79

$$\mathbf{F} = \mathbf{F}_m \mathbf{F}_{pre}. \quad (2)$$

80 The interstitial fluid component of Cauchy stress \mathbf{T}_i takes the form based on the Donnan
 81 equilibrium theory^[15, 34, 35], that is,

$$\mathbf{T}_i = -(p - p^*)\mathbf{I} = -R\theta \left[\sqrt{(c^F)^2 + (\bar{c}^*)^2} - \bar{c}^* \right] \mathbf{I} \quad (3)$$

82 where \mathbf{I} is the identity tensor, p^* is the ambient pressure in the external bath (henceforth
 83 considered to be zero, $p^* = 0$), \bar{c}^* is the external bath salt osmolarity, R is the universal gas
 84 constant, and θ is absolute temperature, c^F is the proteoglycan fixed-charge density relating
 85 to the solid matrix relative volume change ($J = \det \mathbf{F}$) via

$$c^F = \frac{\varphi_0^w c_0^F}{J - 1 + \varphi_0^w} \quad (4)$$

86 where c_0^F and φ_0^w are the fixed-charge density and water content, respectively. Note that in
 87 this paper the above chemical parameters are assumed to be homogeneous.

88 For the solid matrix component, consider an isotropic neo-Hookean constitutive relation-
 89 ship^[36]:

$$\mathbf{T}_s = \mu J^{-5/3} \left(\mathbf{B} - \frac{1}{3} I_1 \mathbf{I} \right) + \kappa (J - 1) \mathbf{I} \quad (5)$$

90 where $\mathbf{B} = \mathbf{F}\mathbf{F}^T$ is the left Cauchy-Green deformation tensor, I_1 is the first invariant of
 91 the right Cauchy-Green deformation tensor \mathbf{C} , and μ and κ are the shear modulus and bulk
 92 modulus of the solid matrix, respectively.

93 In this paper, the reference configuration is set as the zero osmotic loading stage, and
 94 a conceptual sequence of configurations is assumed as shown in Fig. 1 according to Kandil
 95 et al.^[14], in which the stress-free chemical configuration is an intermediate virtual state due
 96 to osmotic swelling. In this way, the total deformation is divided into chemical-induced and
 97 mechanical-induced parts. Note that a non-zero prestretched deformation \mathbf{F}_{pre} is produced
 98 to maintain the Cauchy stress $\mathbf{T} = \mathbf{0}$ in the stress-free chemical configuration. By combining
 99 the Eq.(3), Eq.(4) and Eq.(5), and note that the prestretch \mathbf{F}_{pre} has the form

$$\mathbf{F}_{pre} = \lambda_{pre} \mathbf{I} = (J_{pre})^{1/3} \mathbf{I} \quad (6)$$

100 where $J_{pre} = \det \mathbf{F}_{pre}$, we have the equation for solving \mathbf{F}_{pre} as

$$-p + \kappa (J_{pre} - 1) = 0. \quad (7)$$

101 Finally, the prestretch can be calculated as

$$\mathbf{F}_{pre} = \left(1 + \frac{p}{\kappa} \right)^{1/3} \mathbf{I}. \quad (8)$$

102 *2.2. General principle for VFM*

103 The virtual fields method (VFM) is based on the principle of virtual work, for quasi-static
 104 conditions with neglecting the acceleration and the body force^[20], which may be written such
 105 as,

$$- \int_{\Omega} \mathbf{T} : \boldsymbol{\varepsilon}^* d\Omega + \int_{\partial\Omega_t} \mathbf{t} \cdot \mathbf{u}^* d\partial\Omega_t = 0 \quad (9)$$

106 where \mathbf{T} is the actual Cauchy stress tensor across the domain of interest Ω and is related to
 107 the strains through constitutive equations, strains are derived from gradients of the measured
 108 displacement field \mathbf{u} , \mathbf{t} are the tractions applied on a part of the boundary $\partial\Omega_t$, \mathbf{u}^* is a
 109 kinematically admissible virtual displacement field, and $\boldsymbol{\varepsilon}^*$ is the associated virtual strain
 110 field.

111 First, a constitutive model is chosen, one can write in the general case

$$\mathbf{T} = \mathcal{G}(\boldsymbol{\varepsilon}), \quad (10)$$

112 where \mathcal{G} is a given function of the actual strain components. The constitutive parameters
 113 are also involved in \mathcal{G} . Therefore Eq.(9) can be written as

$$- \int_{\Omega} \mathcal{G}(\boldsymbol{\varepsilon}) : \boldsymbol{\varepsilon}^* d\Omega + \int_{\partial\Omega_t} \mathbf{t} \cdot \mathbf{u}^* d\partial\Omega_t = 0 . \quad (11)$$

114 Then, virtual fields are chosen. Each virtual field introduced into equation Eq.(26) yields
 115 one scalar equation. The constitutive parameters are then sought as solutions to a set of such
 116 equations. The construction of the virtual fields is a key issue of the method. An important
 117 feature is the fact that the above equation is verified for any kinematically admissible virtual
 118 field \mathbf{u}^* ^[20]. Kinematically admissible means that \mathbf{u}^* must be continuous across the whole
 119 volume and it must be equal to the prescribed displacement on the boundary. The virtual
 120 field \mathbf{u}^* can be constructed analytically or solving equations created automatically^[37]. The
 121 detailed procedure of constructing virtual field for the proposed model in this paper will be
 122 introduced later.

123 *2.3. The adaptation of the VFM to biphasic hyperelasticity*

124 *2.3.1. Governing equations*

125 Assuming quasi-static conditions and no body forces^[30], the VFM equations for the
 126 biphasic hyperelasticity can be written as

$$- \int_{\Omega} (\mathbf{T}_i + \mathbf{T}_s) : \boldsymbol{\varepsilon}^* d\Omega + \int_{\partial\Omega_t} \mathbf{t} \cdot \mathbf{u}^* d\partial\Omega_t = 0 \quad (12)$$

127 where \mathbf{T}_s and \mathbf{T}_i denotes the solid matrix component and interstitial fluid component for
 128 actual Cauchy stress across the domain of interest, respectively, \mathbf{t} are the tractions applied
 129 on the boundary $\partial\Omega_t$, Ω is the domain volume in the current configuration, and $\boldsymbol{\varepsilon}^*$ is the
 130 virtual strain field.

131 *2.3.2. Definition of virtual strain fields*

132 In this paper, the virtual displacement fields are defined by solving a serial of equations.
 133 Firstly it is assumed that the osmotic pressure terms vanish under the principle of virtual
 134 work with the use of some special virtual fields, i.e. a special virtual field with $tr(\boldsymbol{\varepsilon}^*) = 0$,
 135 yielding

$$\int_{\Omega} -p(J)\mathbf{I} : \boldsymbol{\varepsilon}^* d\Omega = 0 . \quad (13)$$

136 Further if we consider a three-layers arterial wall tissue for example, including intima,
 137 media and adventitia. Then, Eq.(12) can be written as

$$-\sum_{i=1}^3 \int_{\Omega_i} \mathbf{T}(\mu_i) : \boldsymbol{\varepsilon}^* d\Omega + \int_{\partial\Omega_t} \mathbf{t} \cdot \mathbf{u}^* d\partial\Omega_t = 0 \quad (14)$$

138 where Ω_i is the domain of the i -th layer, and μ_i is the shear modulus in Ω_i .

139 In order to construct the virtual strain fields $\boldsymbol{\varepsilon}^*$ in Eq.(13) a simple approach is to con-
 140 struct a linear virtual displacement field to produce a constant virtual strain field,

$$\mathbf{u}^* = (\eta_1 x)\mathbf{e}_x + (\eta_2 y)\mathbf{e}_y + (\eta_3 z)\mathbf{e}_z . \quad (15)$$

141 where it is required to make $\eta_1 + \eta_2 + \eta_3 = 0$ for meeting Eq.(13).

142 For the case of identification for multi-layers in Eq.(14), the virtual fields are required to
 143 be linearly independent when there are many unknown parameters to be identified simul-
 144 taneously, and in order to realize $tr(\boldsymbol{\varepsilon}^*) = 0$, these more complicate virtual fields can be
 145 constructed by defining the curl of a potential vector field \mathbf{H} ^[37]

$$\mathbf{u}^* = \nabla \times \mathbf{H} , \quad (16)$$

146 since the divergence of the curl above always yields

$$div(\nabla \times \mathbf{H}) = 0 , \quad (17)$$

147 where $\mathbf{H} = H_i \mathbf{e}_i (i = x, y, z)$ and \mathbf{e}_i is the unit vector in the global cartesian coordinate
 148 system.

149 Thus, we can reconstruct virtual displacement fields such as

$$\mathbf{u}^* = \nabla \times \mathbf{H} = \left(\frac{\partial H_z}{\partial y} - \frac{\partial H_y}{\partial z} \right) \mathbf{e}_x + \left(\frac{\partial H_x}{\partial z} - \frac{\partial H_z}{\partial x} \right) \mathbf{e}_y + \left(\frac{\partial H_y}{\partial x} - \frac{\partial H_x}{\partial y} \right) \mathbf{e}_z . \quad (18)$$

150 In this work, under the kinematically admissible condition, we calculated the virtual
 151 displacement field by assuming a special case in an uniaxial tension for a plate as shown
 152 in Fig. 2, where displacement boundary condition is $u_x|_{x=0} = u_y|_{y=0} = u_z|_{z=0} = 0$ which is
 153 usually used, and define the virtual fields as follow:

$$u_x^* = \frac{\partial H_z}{\partial y} - \frac{\partial H_y}{\partial z} = \eta x^k f(z) \quad (19)$$

$$u_y^* = \frac{\partial H_x}{\partial z} - \frac{\partial H_z}{\partial x} = 0 \quad (20)$$

$$u_z^* = \frac{\partial H_y}{\partial x} - \frac{\partial H_x}{\partial y} = \eta z^{k+1} g(x) , \quad (21)$$

154 where k is the exponent parameter of the power functions, η is a scaling factor parameter
 155 which is usually set to a small value to prevent excessive virtual deformation, $f(z)$ and $g(x)$
 156 are undetermined functions. Note that power functions are used for the virtual displacements
 157 in Eq.(19) and (21). The purpose of power functions is to generate virtual strain fields that
 158 avoid linear dependent VFM equations.

159 In order to simply the problem, we set $H_y = 0$, in this way H_x and H_z can be directly
 160 calculated by integration leading to

$$H_x = -\eta y \cdot z^{k+1} g(x) \quad (22)$$

$$H_z = \eta y \cdot x^k f(z) . \quad (23)$$

161 Then, by substituting Eqs.(22) and (23) into Eq.(20), we can deduce that

$$g(x) = -kx^{(k-1)} \quad (24)$$

$$f(z) = (k+1)z^k . \quad (25)$$

162 Finally, combining Eqs.(19), (20), (21), (24) and (25), we obtain the general equations
 163 for these special virtual fields such as

$$\begin{cases} u_x^* = \eta(k+1)x^k z^k \\ u_y^* = 0 \\ u_z^* = -\eta k x^{k-1} z^{k+1} . \end{cases} \quad (26)$$

164 2.3.3. Summary of the complete procedure

165 Based on the theory and methods introduced above, the procedure for the implementation
 166 of the proposed model is briefly shown in Table 1, mainly including three parts in the
 167 following:

168 (1)**Full-field measurements:** The displacement fields used in this study have three
 169 different possible origins, namely analytical solutions, FE analyses and real experiments. For
 170 simple homogeneous (monolayer) uniaxial tension, the analytical solution can be used. For a
 171 multilayered structure, the FEM is used to provide simulated measurements and derive the
 172 deformation gradient \mathbf{F} and the Jacobian J . For the experimental case, the displacements
 173 are measured using optical coherence tomography (OCT) and digital volume correlation
 174 (DVC) before deducing \mathbf{F} , \mathbf{E} and J , The traction \mathbf{t} for the VFM in numerical verifications is
 175 pointwise on the boundary, but as for experiment case, the measured stress is an average force
 176 by assuming cross-section perfectly homogeneous as it is hard to measure the heterogeneous
 177 traction distribution on the boundary in the experiment.

178 (2)**Building the VFM equations:** From the obtained \mathbf{F} fields, we determine \mathbf{T} ac-
 179 cording to Eq.(1),(3),(4),(5). Special virtual fields based on Eq.(26) are applied to Eq.(14).
 180 Since \mathbf{T} depends on the unknown parameters $\boldsymbol{\mu}$, the virtual work equation Eq.(14) is not
 181 satisfied exactly, and a residual can be derived, as defined in Eq.(27). This residual is then
 182 minimized. The cost function can be written such as

$$f(\mu_1, \mu_2, \mu_3) = \sum_{v=1}^3 \left[- \sum_{i=1}^3 \int_{\Omega_i} \mathbf{T} : \boldsymbol{\varepsilon}^{*v} d\Omega + \int_{\partial\Omega} \mathbf{t} \cdot \mathbf{u}^{*v} d\partial\Omega \right]^2, \quad (27)$$

183 which represents the quadratic deviation between the internal virtual work (IVW) and the
 184 external virtual work (EVW), with v labelling the virtual field and i labelling the layer.

185 Using Gauss quadrature in isoparametric elements, integrals in the cost function can be
 186 changed into discrete sums, such as

$$f(\mu_1, \mu_2, \mu_3) = \sum_{v=1}^3 \left[- \sum_{i=1}^3 \sum_{ele} \mathbf{T}(\mu_i, \mathbf{X}^{ele}) : \boldsymbol{\varepsilon}^{*v}(\mathbf{X}^{ele}) + \sum_{eleb} t^{eleb} A^{eleb} \mathbf{u}^{*v}(\mathbf{X}^{eleb}) \right]^2 \quad (28)$$

187 where ele and $eleb$ denote the element and boundary element respectively, A^{eleb} is the area
 188 of one element side, $\boldsymbol{\varepsilon}^{*v}(\mathbf{X}^{ele})$ denotes the value of the v -th virtual strain field at the Gauss
 189 integration point in the ele -th element, and $\boldsymbol{\varepsilon}^{*v}$ is derived from \mathbf{u}^{*v} .

190 (3) **Solving the VFM equations:** We use the MATLAB *fminsearch* function to
 191 search for $\boldsymbol{\mu}$, in which the derivative-free Nelder-Mead simplex optimization algorithm is
 192 used for finding the minimum value of an unconstrained multivariable scalar function^[38].
 193 The problem can be expressed as

$$\begin{cases} \text{Find } \boldsymbol{\mu} = \{\mu_1, \mu_2, \mu_3\} \\ f(\boldsymbol{\mu}) = \sum_{v=1}^3 (-W_v^{\text{In}} + W_v^{\text{Ex}})^2 \\ \min f(\boldsymbol{\mu}) \end{cases} \quad (29)$$

194 where W_v^{In} represents the IVW under the v -th virtual field, and W_v^{Ex} represents the EVW
 195 under the v -th virtual field. Eventually, the cost function is minimized through an iterative
 196 scheme and yields the unknown material parameters.

Table 1: Steps of the identification procedure for biphasic hyperelastic parameters

-
1. Forward simulation of chemomechanically coupled model and experimental tests in osmotically active solution.
 2. Acquisition of full-field displacement from numerical calculation or experimental measurements.
 3. Computation of deformation gradient \mathbf{F} through the given full-field displacement.
 4. Computation Cauchy stress \mathbf{T} from chemomechanically constitutive equations.
 5. Choice of virtual field that satisfies $tr(\boldsymbol{\varepsilon}^*) = 0$ to avoid the effect of the chemo term.
 6. Computation of the value of cost function f .
 7. Use of the optimization method to find a vector of $\boldsymbol{\mu}$ by minimizing f .
 8. Checking whether the identified value equals the parameters used in forward simulation.
-

197 2.3.4. Noise investigation method

198 In order to study the influence of measurement errors on identifications, we add artificial
 199 white noise to the displacement data obtained by the FEM simulations as^[39].

$$u_i^{a,n} = u_i^{a,\text{fem}} + \delta_i^{a,\Delta n} \quad \text{with} \quad \delta_i^{a,\Delta n} \sim \mathcal{N}(0, \sigma_u^2) \quad \forall (a, i) \in \Omega \quad (30)$$

200 where $u_i^{a,\text{fem}}$ and $\delta_i^{a,\Delta n}$ denote the true displacement from FEM and random noise, respec-
 201 tively, the $\delta_i^{a,\Delta n}$ represents the Gaussian white noise with zero mean and standard deviation
 202 σ_u ranging between 10^{-4} (low noise) to 10^{-3} (high noise)^[40]. For each fixed value of σ_u , 40
 203 realizations of Gaussian white noise $\delta_i^{a,\Delta n}$ were generated. The average identified results for
 204 all the samples were calculated^[41].

205 The relative error was defined as

$$\text{error} = \frac{\hat{\mu}_i - \bar{\mu}_i}{\hat{\mu}_i} \times 100\% \quad (31)$$

206 where $\hat{\mu}_i$ and $\bar{\mu}_i$ are the exact shear modulus and average identified value under 40 samples
 207 respectively.

208 2.4. Verification of the new VFM based on analytical or FEM simulations

209 In this paper, the proposed model as established in previous section will be verified in
 210 theoretical cases before applying into the practical problems. In the verification, the full-
 211 filled measurements are assumed to be 'virtually' obtained from analytical solutions or FE
 212 analyses. The derivations for analytical solutions and FE schemes are introduced in the
 213 following, respectively.

214 2.4.1. Analytical solution for a plate under tension

215 For some cases with simple geometry and boundary conditions, the analytical solution
 216 of the biphasic hyperelastic problem can be derived. For example, consider a plate under
 uniaxial tension, as shown in Fig. 2, where λ is the prescribed axial stretch, and α and β are

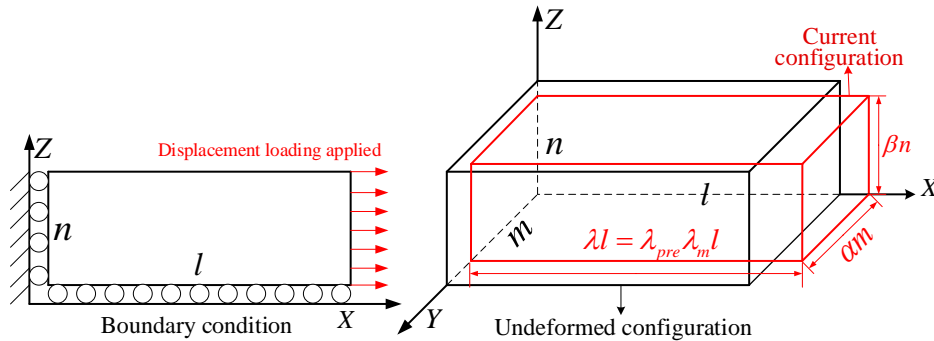


Figure 2: The geometry and boundary conditions for a plate under tension

217 unknowns, then total deformation is
 218

$$\mathbf{F} = \begin{bmatrix} \lambda & 0 & 0 \\ 0 & \alpha & 0 \\ 0 & 0 & \beta \end{bmatrix}. \quad (32)$$

219 Under this uniaxial tension case, according to Eq.(1),(3),(4),(5), we could have

$$T_{22} = -p + \mu(\lambda\alpha\beta)^{-5/3}\left(\frac{2}{3}\alpha^2 - \frac{1}{3}\lambda^2 - \frac{1}{3}\beta^2\right) + \kappa(\lambda\alpha\beta - 1) = 0 \quad (33)$$

$$T_{33} = -p + \mu(\lambda\alpha\beta)^{-5/3}\left(\frac{2}{3}\beta^2 - \frac{1}{3}\lambda^2 - \frac{1}{3}\alpha^2\right) + \kappa(\lambda\alpha\beta - 1) = 0 . \quad (34)$$

220 The relationship $\alpha = \beta$ can be derived from the equations above, therefore the Eq.(34)
221 can be rewritten as

$$T_{33} = -p + \mu(\lambda\beta^2)^{-5/3}\left(\frac{1}{3}\beta^2 - \frac{1}{3}\lambda^2\right) + \kappa(\lambda\beta^2 - 1) = 0 \quad (35)$$

222 where p based on Eq.(3) and (4), can be elaborated as

$$p = \left(R\theta \left[\sqrt{\left(\frac{\varphi_0^w c_0^F}{\lambda\beta^2 - 1 + \varphi_0^w}\right)^2 + (\bar{c}^*)^2} - \bar{c}^* \right] + p^* \right) . \quad (36)$$

223 To solve this nonlinear problem, the Newton method is applied, yielding

$$\beta_{n+1} = \beta_n - \frac{T_{33}(\beta_n)}{T'_{33}(\beta_n)} \quad (37)$$

224 where β_n is the n -th iteration of β . For any λ , β and α , hence \mathbf{F} can be deduced with this
225 iterative resolution.

226 2.4.2. FEM solutions

227 The FEM is an alternative approach when analytical resolution is not possible. Let
228 $\mathbf{x} = \boldsymbol{\varphi}(\mathbf{X}, t)$ describe the motion of a body from the initial reference configuration $\mathbf{X} \in k(0)$
229 to its current configuration $\mathbf{x} \in k(t)$. Define the deformation gradient as

$$\mathbf{F} = \nabla_{\mathbf{X}} \boldsymbol{\varphi} . \quad (38)$$

230 The general total potential energy for the biphasic hyperelasticity model is

$$\Pi = \int_{\Omega} \Psi d\Omega - \int_{\Omega} \bar{\mathbf{b}} \cdot \boldsymbol{\varphi} d\Omega - \int_{\partial\Omega} \bar{\mathbf{t}} \cdot \boldsymbol{\varphi} d\partial\Omega . \quad (39)$$

231 where Ψ is the strain energy, $\bar{\mathbf{b}}$ is the body force vector per unit current volume of Ω and $\bar{\mathbf{t}}$
232 are the tractions on the boundary $\partial\Omega$.

233 Minimization of the potential energy with respect to $\boldsymbol{\varphi}$ results in a nonlinear system of
234 equation, and the variational forms in the spatial description are

$$\int_{\Omega} \mathbf{T} : \nabla_{\mathbf{x}} \delta \boldsymbol{\varphi} d\Omega - \int_{\Omega} \bar{\mathbf{b}} \cdot \delta \boldsymbol{\varphi} d\Omega - \int_{\partial\Omega} \bar{\mathbf{t}} \cdot \delta \boldsymbol{\varphi} d\partial\Omega = 0 . \quad (40)$$

235 In finite element discretization, isoparametric interpolations of geometry variables \mathbf{X} and
 236 field variables $\boldsymbol{\varphi}$ are written as

$$\mathbf{X} = \sum_{I=1}^n N_I(\xi) \mathbf{X}_I, \quad \boldsymbol{\varphi} = \sum_{I=1}^n N_I(\xi) \boldsymbol{\varphi}_I \quad (41)$$

237 where ξ denotes the coordinates in the reference element, and n is the number of nodes in
 238 each element.

239 Substituting Eq.(41) into Eq.(40) and using the Newton-Raphson scheme to solve the
 240 nonlinear system of equations^[42], we obtain

$$\mathbf{R}_\varphi^i + \mathbf{K}_\varphi^i \cdot \Delta \boldsymbol{\varphi}^{i+1} = \mathbf{0} \quad (42)$$

241 where \mathbf{R}_φ is the global residual vector, and the element stiffness matrix is given by

$$\mathbf{K}_\varphi = \int_{\Omega} \nabla_x^T \mathbf{N} \cdot \mathbf{C} \cdot \nabla_x \mathbf{N} d\Omega + \int_{\Omega} [\nabla_x^T \mathbf{N} \cdot \mathbf{T} \cdot \nabla_x \mathbf{N}] \mathbf{I} d\Omega \quad (43)$$

242 and the spatial elasticity tensor \mathbf{C} is given by

$$\mathbf{C} = \mathbf{C}^{osmo} + \mathbf{C}^e \quad (44)$$

243 where \mathbf{C}^e is the spatial elasticity tensor for the solid matrix, which can be written as

$$\mathbf{C}^e = 4J^{-1}(\mathbf{F} \underline{\otimes} \mathbf{F}) : \frac{\partial^2 W}{\partial \mathbf{C}^2} : (\mathbf{F}^T \underline{\otimes} \mathbf{F}^T) \quad (45)$$

244 in which $\mathbf{C} = \mathbf{F}^T \mathbf{F}$ is the right Cauchy-Green deformation tensor, and W is a strain energy
 245 density function for the solid. Here, a hyperelastic constitutive model^[36] is used and is
 246 expressed as

$$W = \frac{1}{2} \mu (J^{-2/3} I_1 - 3) + \frac{1}{2} \kappa (J - 1)^2 \quad (46)$$

247 and \mathbf{C}^{osmo} in Eq.(44) is the tensor of the osmotic modulus,

$$\begin{aligned} \mathbf{C}^{osmo} &= J^{-1}(\mathbf{F} \underline{\otimes} \mathbf{F}) : 2 \frac{\partial (-Jp\mathbf{C}^{-1})}{\partial \mathbf{C}} : (\mathbf{F}^T \underline{\otimes} \mathbf{F}^T) \\ &= -J \frac{\partial p}{\partial J} \mathbf{I} \otimes \mathbf{I} + p(2\mathbf{I} \underline{\otimes} \mathbf{I} - \mathbf{I} \otimes \mathbf{I}) \end{aligned} \quad (47)$$

248 which results in part from the change in osmotic pressure with a change in tissue volume^[9, 33].
 249 The detailed expression of \mathbf{C}^{osmo} can be found in Azeloglu et al.^[15].

250 *2.5. Application to experimental data*

251 Uniaxial tensile tests were previously performed to stimulate and investigate chemoelastic
 252 effects in arteries^[17]. In these experiments, porcine descending thoracic aortas were excised
 253 and used as test samples. Propylene glycol (PG) and phosphate-buffered saline (PBS) were
 254 mixed to prepare an osmotically active solution.

255 Three rectangular samples ($10 \times 58\text{mm}$), named Aorta1, Aorta2 and Aorta3, were im-
 256 mersed in an 80% PG solution and tested in uniaxial tension (stepwise stress-relaxation
 257 tests). The loading direction was aligned with (Y-axis). Strain fields were measured dur-
 258 ing these tests using optical coherence tomography (OCT) and digital volume correlation
 259 (DVC)^[16].

260 Before carrying out the stepwise uniaxial tensile tests, a 1.15 stretch preconditioning
 261 (displacement increment of 5.2mm) was applied. The initial distance between clamps was
 262 35.1mm, as shown in Fig. 3.

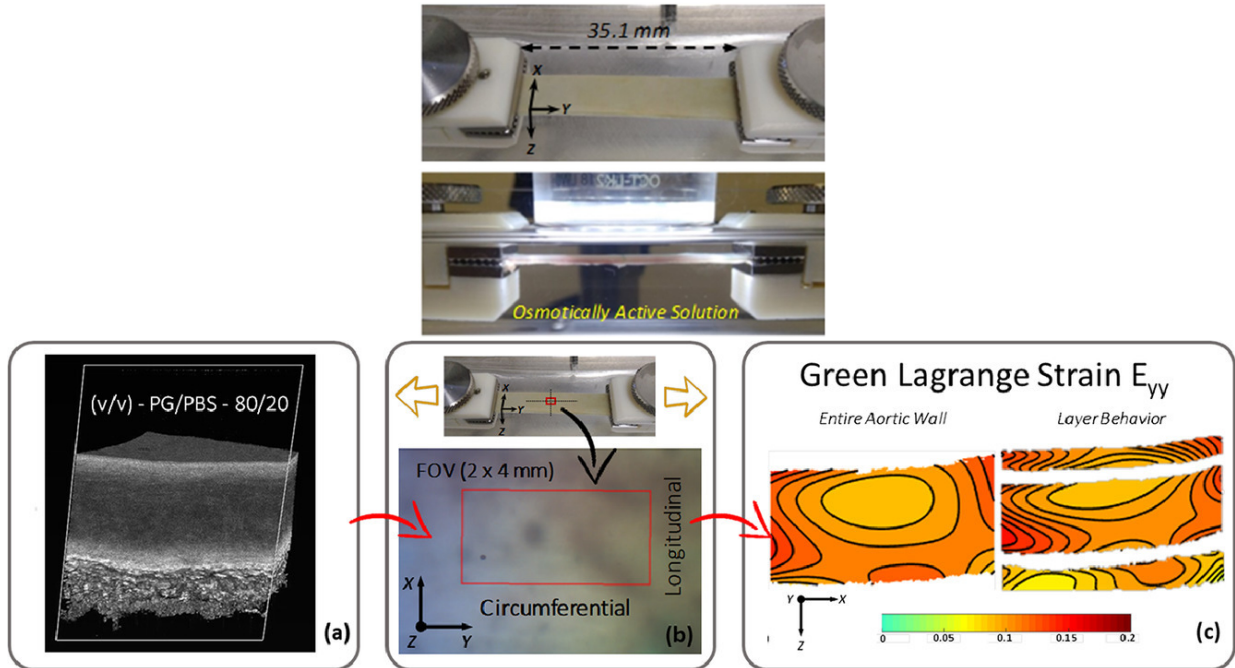


Figure 3: Setup used for obtaining experimental datasets and acquisitions of experimental data using the OCT-DVC technique^[17]

263 OCT volumetric images were acquired under a field of view (FOV) of $2 \times 4 \times 2.51\text{mm}$
 264 (X-, Y- and Z-axes, respectively, see Fig. 3(b)). Four specific regions of interest were defined
 265 on the OCT volume images: the entire aortic wall (global), the intima region, the media
 266 region and the adventitia region. 3D displacement fields were measured using DVC with
 267 a local correlation algorithm (LA-DVC). Ideal correlation conditions were reached directly
 268 in the 3D OCT image sequence acquisition and using a rigid body translation test. The
 269 implemented correlation parameters can be found in our previous work^[16, 17]. The voxel size

270 was a key parameter to reduce the uncertainties of the full-field measurements. The subset
 271 size parameter was used as (128, 96, 64, 32, 16, and 8 voxels). After measuring and fitting
 272 the displacement fields with tricubic functions, the components of the Green–Lagrange strain
 273 tensor were calculated with MatLab[®]. Here the error of measurement is not considered and
 274 only the mean value of displacement measurement is used for simplification.

275 3. Results

276 3.1. First case study: homogeneous material with uniaxial tension

277 This first case study is a plate under uniaxial tension, as introduced in Section 2.4.1,
 278 where an analytical solution is derived. A stretch λ is applied in the x direction at the
 279 right-side of the plate, and the constraints are applied as shown in Fig. 2. The parameters
 of the chemo-mechanically coupled constitutive model are reported in Table 2.

Table 2: Parameters of the chemo-mechanically coupled constitutive model

Type	Description	Symbol	Values	Units
	Universal gas constant	R	8.314	$\text{kg} \cdot \text{m}^2\text{s}^{-2}\text{K}^{-1}\text{mol}^{-1}$
	Absolute temperature	θ	298	K
Chemoelastic term	Ambient pressure	p^*	0	kPa
	Initial fixed-charge density	c_0^F	[20,40,100,200]	meq/L
	Water content	φ_0^w	70	%
	External bath salt osmolarity	\bar{c}^*	[10-2000]	mosM
Hyperelastic	Shear modulus	μ	140	kPa
	Bulk modulus	κ	1400	kPa

280

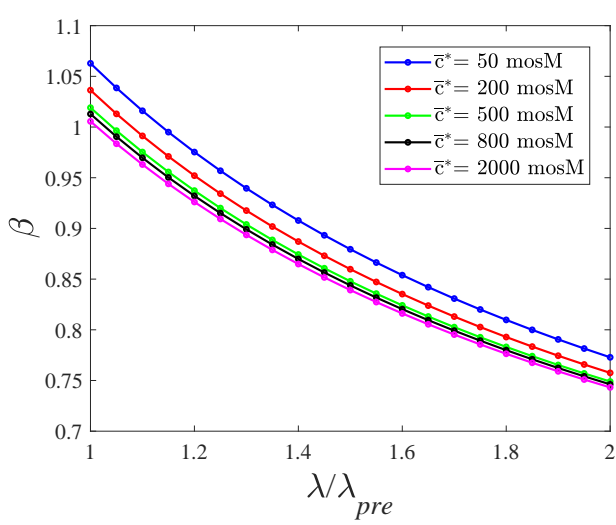
281 3.1.1. Analytical solutions

282 Based on the analytical solutions of Section 2.4.1, the solutions of deformation and stress
 283 are shown in Fig. 4. The deformation in Y-direction β is shown in Fig. 4(a) with different
 284 external bath salt osmolarity \bar{c}^* , and it is seen that a larger β is produced with a lower \bar{c}^*
 285 because of a larger swelling. The influences of \bar{c}^* on total Cauchy stress T_{11} is illustrated in
 286 Fig. 4(b), in which a smaller external bath salt osmolarity produces a relatively smaller total
 287 T_{11} , it can be explained that as the T_{11} has hyperelastic part and chemo part according to
 288 Eqs.(3),(5), while the chemo part p will be increased with a lower \bar{c}^* as shown in Fig. 4(c),
 289 therefore, a lower total Cauchy stress is produced.

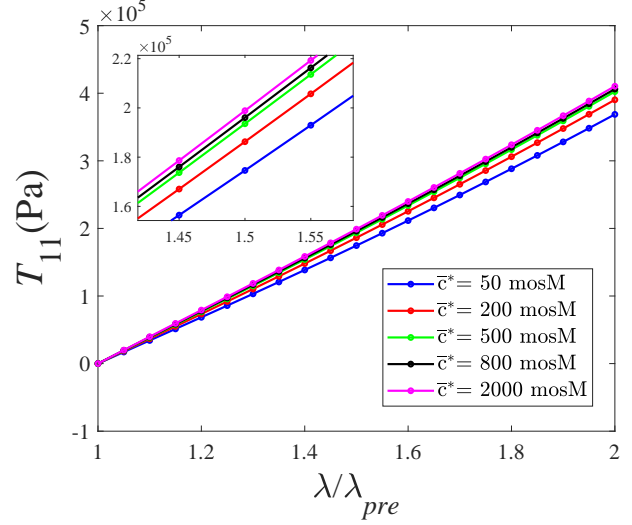
290 3.1.2. Parameter identification

291 Since the material considered in the first case study is homogeneous, there is only one
 292 unknown parameter, μ . Thus, one single linear virtual displacement field based on Eq.(15)
 293 is considered, that is,

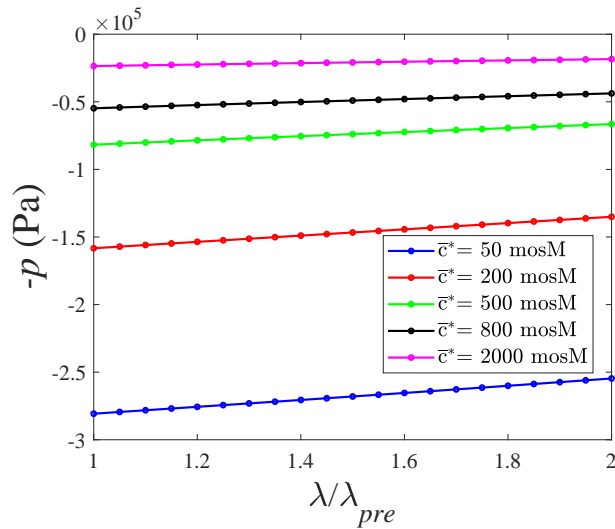
$$\mathbf{u}^* = \begin{bmatrix} 0.2x \\ -0.1y \\ -0.1z \end{bmatrix} \quad \boldsymbol{\varepsilon}^* = \begin{bmatrix} 0.2 & & \\ & -0.1 & \\ & & -0.1 \end{bmatrix}. \quad (48)$$



(a)



(b)



(c)

Figure 4: Analytical results under different external bath salt osmolarities and initial fixed-charge density $c_0^F = 200$ meq/L in uniaxial tension. (a) Stretch β variation in the Z-direction. (b) Cauchy stress T_{11} . (c) Osmotic pressure p .

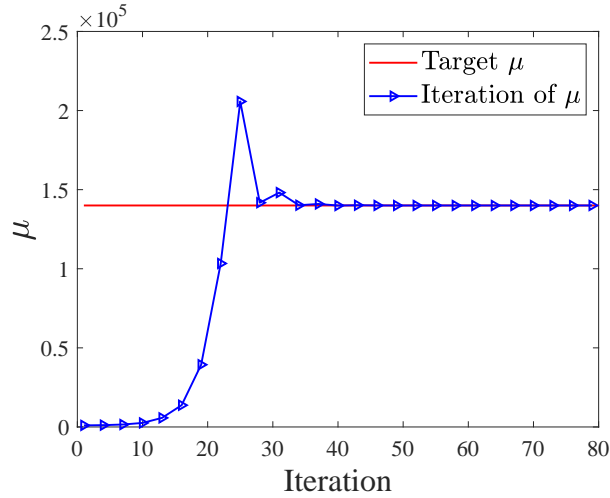


Figure 5: The process of convergence for the shear modulus in the identification.

294 The shear modulus in solid part is well identified as shown in Table 3 regardless the
 295 existence of chemo term and the convergence process of μ is shown in Fig. 5. Due to many
 296 uncertainties in the chemo terms, we verify that the proposed VFM is immune to chemoelas-
 297 tic coupling effects by simulating three different external bath salt osmolarity environments
 298 and one different initial fixed-charge density in the tissue. The identified results of shear
 299 modulus $\tilde{\mu}$ are always equal to the exact shear modulus $\hat{\mu}$, as reported in Table 3. Moreover,
 300 we also test the identification results under different initial guess values and target(exact)
 301 values, the results are provided in Table 4, in which the initial values of shear modulus μ
 302 changes from 1000 Pa to 10000 Pa and the exact value of shear modulus $\hat{\mu}$ changes from
 303 130000 Pa to 150000 Pa, it is shown that the identified results maintain a good accuracy
 304 with relative error less than 1%.

305 Based on the noise analysis method in Section 2.3.4, we tested the influence of noise on
 306 the identification, as reported in Table 5. It is shown that the error remains less than 3%,
 307 with a relatively low noise level ($\sigma_u \leq 5 \times 10^{-4}$) but gradually increases with the increase of
 noise level.

Table 3: Identified shear modulus in the first case study

Type	Symbol	Value			
External bath salt osmolarity	\bar{c}^*	50 mosM	100 mosM	500 mosM	500 mosM
Initial fixed-charge density	c_0^F	40 meq/L	40 meq/L	40 meq/L	60 meq/L
Tensile stretch	λ	1.2	1.2	1.2	1.2
Initial guess shear modulus	μ	1000Pa	1000Pa	1000Pa	1000Pa
Identified modulus	$\tilde{\mu}$	140000Pa	140000Pa	140000Pa	140000Pa
Exact modulus	$\hat{\mu}$	140000Pa	140000Pa	140000Pa	140000Pa

308

Table 4: The identification results of different exact values and initial guesses

Identified $\tilde{\mu}$ (Pa) and relative error(%)	Exact values $\hat{\mu}$ (Pa)					
	130000	135000	140000	145000	150000	
Initial guess μ (Pa)	1000	129533 (-0.36)	135192 (0.14)	140000 (0)	144500 (-0.34)	150123 (0.08)
	2000	129533 (-0.36)	135192 (0.14)	140000 (0)	144500 (-0.34)	150123 (0.08)
	3000	129533 (-0.36)	135192 (0.14)	140000 (0)	144500 (-0.34)	150123 (0.08)
	4000	129533 (-0.36)	135192 (0.14)	140000 (0)	144500 (-0.34)	150123 (0.08)
	5000	129533 (-0.36)	135192 (0.14)	140000 (0)	144500 (-0.34)	150123 (0.08)
	6000	129533 (-0.36)	135192 (0.14)	140000 (0)	144500 (-0.34)	150123 (0.08)
	7000	129533 (-0.36)	135192 (0.14)	140000 (0)	144500 (-0.34)	150123 (0.08)
	8000	129533 (-0.36)	135192 (0.14)	140000 (0)	144500 (-0.34)	150123 (0.08)
	9000	129533 (-0.36)	135192 (0.14)	140000 (0)	144500 (-0.34)	150123 (0.08)
	10000	129533 (-0.36)	135192 (0.14)	140000 (0)	144500 (-0.34)	150123 (0.08)

Table 5: The relative error of identified results under different levels of measurement noises

Standard deviation σ_u	1×10^{-4}	3×10^{-4}	5×10^{-4}	7×10^{-4}	1×10^{-3}
Exact $\hat{\mu}$ (Pa)	140000	140000	140000	140000	140000
Mean identified $\bar{\mu}$ (Pa)	140349	139443	136382	131183	119993
<i>error</i>	-0.25%	0.4%	2.58%	6.30%	14.29%

309 **3.2. Second case study: multilayer material under biaxial tension**

310 The second case study relies on the chemomechanically coupled constitutive model that
 311 we implemented within the Abaqus/Standard commercial FE software by means of the user
 312 subroutine UMAT, based on Eqs.(3),(4),(5),(45) and (47).

313 The geometry of this second case study is shown in Fig. 6 to simulate the layered structure
 314 of arteries. The size of the three-layers plate is $0.08 \times 0.04 \times 0.03\text{m}$ (i.e. $l=0.08$, $m=0.04$
 315 and $n=0.03$) and the geometry is discretized with a fine mesh of 768 cubic elements. The
 316 boundary conditions are the same as the first case study in Fig. 2, with $u_x|_{x=0} = u_y|_{y=0} =$
 317 $u_z|_{z=0} = 0$. Biaxial displacement loading is applied to the X and Y directions, including
 318 1.30 stretch in X direction and 1.05 stretch in Y direction. Accordingly, the hyperelastic
 319 constitutive model is used for arterial tissues in this example. The values for the constitutive
 320 parameters are those reported in Tables 6. Note here we use a large bulk modulus to make
 321 the material nearly incompressible.

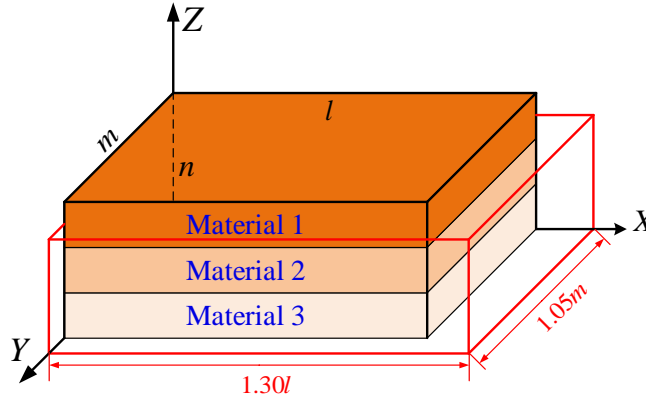


Figure 6: The geometry and displacement loading for the three-layers plate

322 **3.2.1. FEM solutions**

323 Firstly, we verify the accuracy of the FE solutions for direct analysis. As it is not
 324 possible to find the analytical solution for the three-layers examples, so we use the FE
 325 model introduced in Section 2.4.2 to solve the previous first case example with different bath
 326 osmolarity values. As it is shown in Fig. 7, it is found that there is a very good agreement
 327 between FE and analytical solutions.

328 **3.2.2. Parameter identification**

329 For the second case study, we can still consider the constant virtual strain field of Eq.(48),
 330 which is represented in Fig. 8(a). However, two other heterogeneous virtual fields are re-
 331 quired to be introduced to ensure independence among the three VFM equations. Based on
 332 Eq.(26), two other virtual fields can be determined as illustrated in Fig. 8(b) and 8(c) where
 333 parameters setting details can also be found.

Table 6: Parameters of the chemo-mechanically coupled constitutive model for second case study

Type	Description	Symbol	Values	Units	
Chemoelastic term	Universal gas constant	R	8.314	$\text{kg} \cdot \text{m}^2 \text{s}^{-2} \text{K}^{-1} \text{mol}^{-1}$	
	Absolute temperature	θ	298	K	
	Ambient pressure	p^*	0	kPa	
	Initial fixed-charge density	c_0^F	40	meq/L	
	Water content	φ_0^w	70	%	
	External bath salt osmolarity	\bar{c}^*	[20,100,500,1000]	mosM	
Hyperelastic term	Material 1	Shear modulus	μ_1	100	kPa
		Bulk modulus	κ	6000	kPa
	Material 2	Shear modulus	μ_2	200	kPa
		Bulk modulus	κ	6000	kPa
	Material 3	Shear modulus	μ_3	300	kPa
		Bulk modulus	κ	6000	kPa

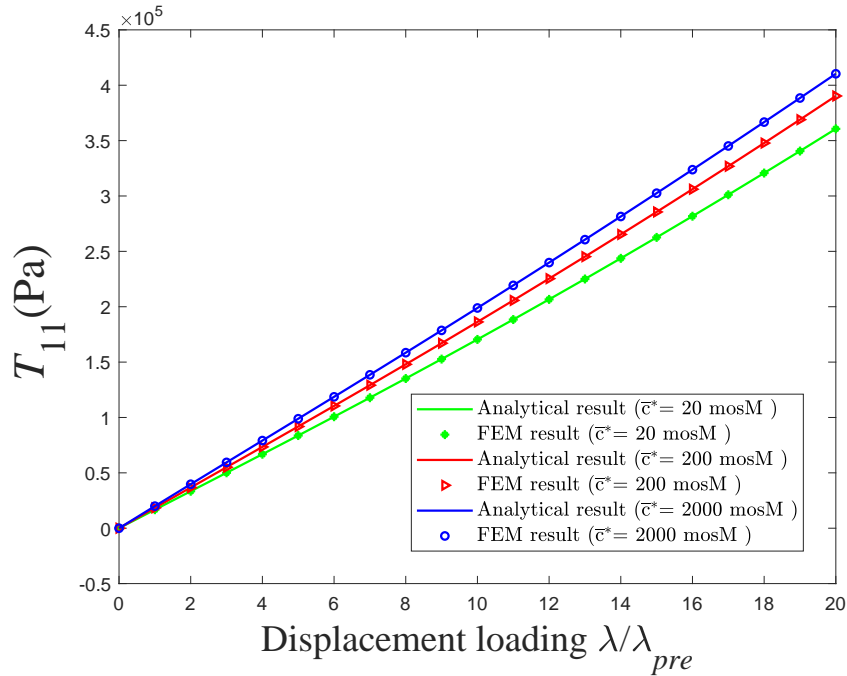


Figure 7: Verification of the FE model against the analytical model on the results of Cauchy stress

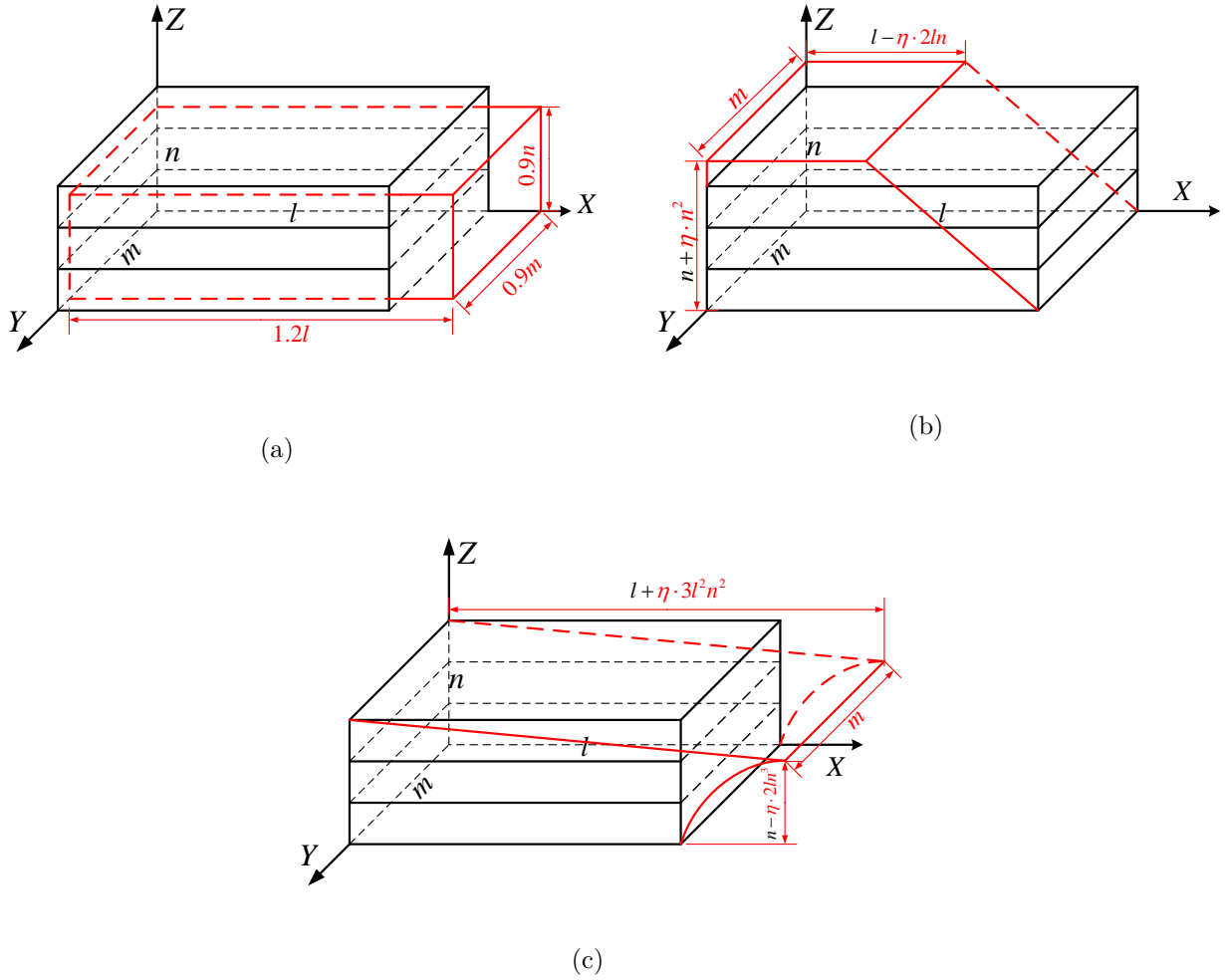
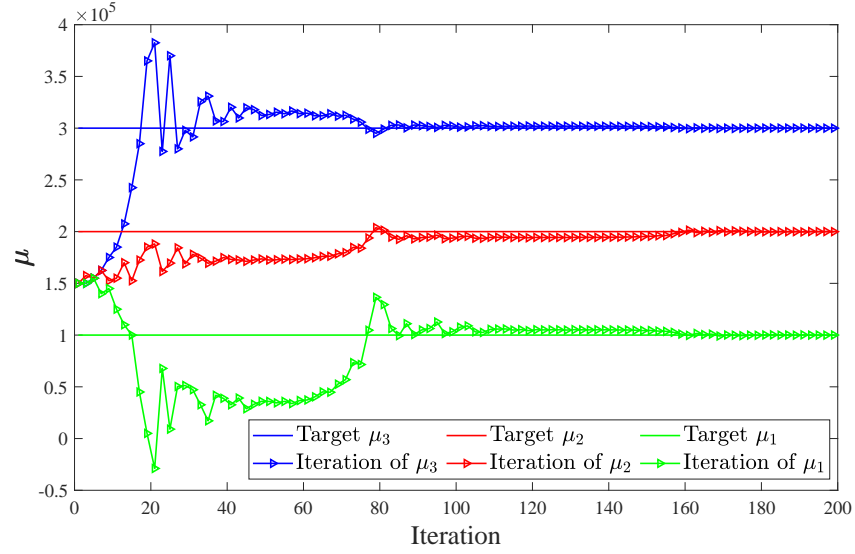
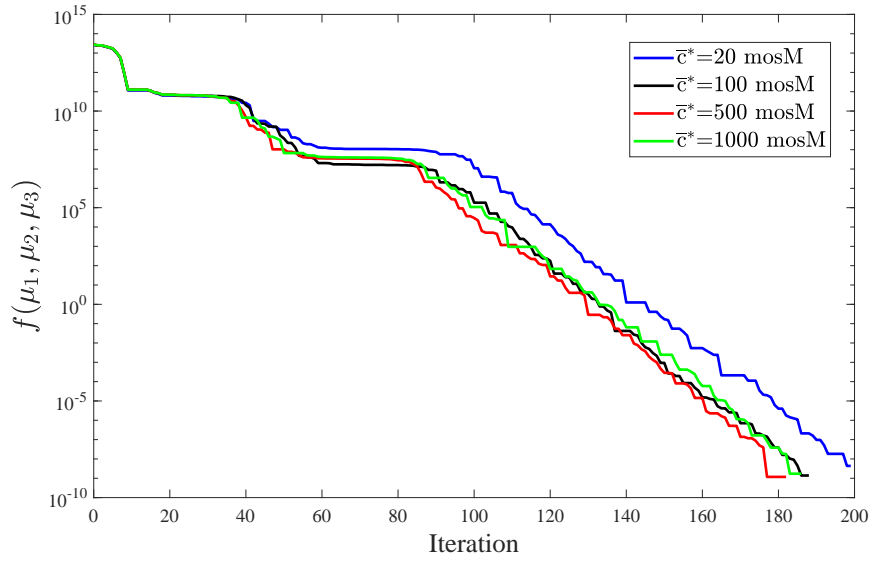


Figure 8: The three virtual displacement fields used in the second case study. (a) Constant strain field. (b) Heterogeneous virtual strain with $k = 1$ and $\eta = -0.01$. (c) Heterogeneous virtual strain with $k = 2$ and $\eta = 0.001$.



(a)



(b)

Figure 9: The identification process in the second case study. (a) Convergence plot of the novel VFM approach for each layer parameter. (b) Cost function f descent.

Table 7: The identified results for different layers under different external bath osmolarities

\bar{c}^*	Type	Material 1	Material 2	Material 3
	Initial value of $\boldsymbol{\mu}$ (Pa)	150000	150000	150000
20 mosM	Identified $\tilde{\boldsymbol{\mu}}$ (Pa)	100000.95	199999.81	299998.34
100 mosM	Identified $\tilde{\boldsymbol{\mu}}$ (Pa)	99999.02	200001.77	300003.04
500 mosM	Identified $\tilde{\boldsymbol{\mu}}$ (Pa)	100001.24	199998.37	299996.26
1000 mosM	Identified $\tilde{\boldsymbol{\mu}}$ (Pa)	99997.62	200001.04	300006.52
	Exact $\hat{\boldsymbol{\mu}}$ (Pa)	100000	200000	300000
	Average relative error (%)	1.388×10^{-3}	5.788×10^{-4}	1.247×10^{-3}

334 The identification for each layer is verified by considering with different chemoelastic
335 terms. As reported in Table 7, the same values of $\boldsymbol{\mu}$ are identified even if we assume different
336 values for the external salt osmolarity. This demonstrates that the proposed model is effective
337 in shear modulus identification without knowing the chemoelastic terms. The process of
338 minimizing the cost function $f(\mu_1, \mu_2, \mu_3)$ is provided in Fig. 9.

339 The influence of noise on the identification is reported in Table 8. The material param-
340 eters are well recovered with a low noise level ($\sigma_u < 5 \times 10^{-4}$) and it is also shown that the
341 error of identified results is increased with the increase of noise level. However, when the
342 noise level reaches a higher level ($\sigma_u = 1 \times 10^{-3}$), the results deviate significantly from the
343 reference values.

Table 8: The relative error of identified results in three layers under different levels of measurement noises

σ_u	Mean identified values $\bar{\boldsymbol{\mu}}$ (Pa)					
	$\bar{\mu}_1$	$error(\%)$	$\bar{\mu}_2$	$error(\%)$	$\bar{\mu}_3$	$error(\%)$
1×10^{-4}	99622.35	0.38	200185.09	-0.09	298801.27	0.40
3×10^{-4}	97340.56	2.66	197091.80	1.45	292038.95	2.65
5×10^{-4}	92950.14	7.05	189106.28	5.45	279275.88	6.91
7×10^{-4}	86117.79	13.88	175407.71	12.30	259909.74	13.36
1×10^{-3}	63550.56	36.45	142574.59	28.71	209265.30	30.24
Exact values	100000.00	—	200000.00	—	300000.00	—

344 3.3. Third case study: uniaxial tensile test of descending thoracic aortas

345 The third example consider the parameter identification based on the measurements
346 in a uniaxial tensile test of descending thoracic aortas described in Section 2.5. Three
347 samples with the same size were tested. The thickness ratio of each layer was set as 1:8:1
348 (adventitia:media:intima), according to the size of experimental sample^[17]. The geometry
349 for the sample is shown in Fig. 10. The measurement for the average Green-Lagrange
350 strains with the standard deviation(std) and the corresponding applied force in the different
351 deformed configurations for each sample are reported in Tables 9, 10, and 11.

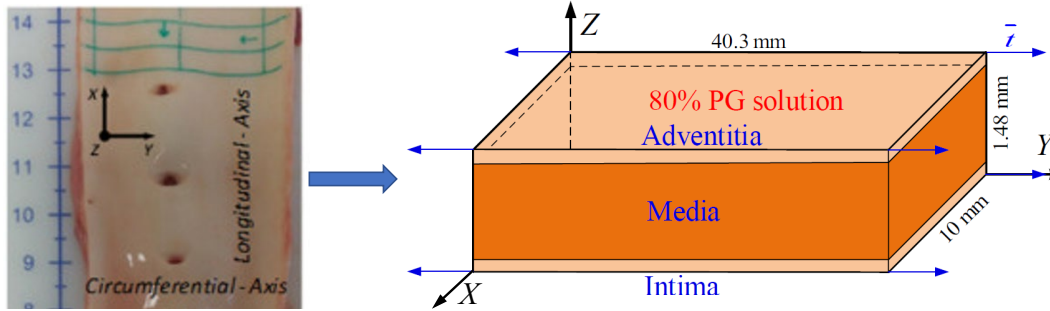


Figure 10: Geometry and boundary condition for an aortic sample immersed in a PG solution and subjected to a uniaxial tensile test

Table 9: The average Green-Lagrange strains from the experiment for Aorta1

Type	Loading step	Measured stress(MPa)	E_{xx} (%) (std)	E_{yy} (%) (std)	E_{zz} (%) (std)
Global	3rd	0.07	-1.510 (0.42)	4.352 (0.26)	0.145 (1.18)
	5th	0.1	-2.124 (0.52)	7.090 (0.37)	0.108 (2.32)
	7th	0.13	-2.596 (0.71)	9.554 (0.51)	0.170 (3.56)
	9th	0.17	-3.125 (0.76)	11.847 (0.60)	0.353 (4.76)
Intima	3rd	0.07	-1.558 (0.42)	4.381 (0.35)	-2.271 (4.57)
	5th	0.1	-2.136 (0.44)	7.157 (0.49)	-3.528 (6.99)
	7th	0.13	-2.600 (0.65)	9.603 (0.67)	-4.768 (8.89)
	9th	0.17	-3.129 (0.74)	11.949 (0.79)	-5.566 (10.18)
Media	3rd	0.07	-1.489 (0.39)	4.376 (0.23)	1.003 (0.34)
	5th	0.1	-2.127 (0.54)	7.112 (0.32)	1.603 (0.63)
	7th	0.13	-2.582 (0.68)	9.570 (0.45)	2.263 (1.60)
	9th	0.17	-3.114 (0.72)	11.857 (0.52)	3.007 (2.67)
Adventitia	3rd	0.07	-1.434 (0.67)	4.273 (0.35)	-2.120 (3.15)
	5th	0.1	-2.043 (0.85)	6.958 (0.46)	-3.525 (4.96)
	7th	0.13	-2.509 (1.05)	9.407 (0.65)	-4.795 (6.73)
	9th	0.17	-3.020 (1.24)	11.630 (0.79)	-6.137 (7.91)

Table 10: The average Green-Lagrange strains from the experiment for Aorta2

Type	Loading step	Measured stress(MPa)	E_{xx} (%) (std)	E_{yy} (%) (std)	E_{zz} (%) (std)
Global	3rd	0.06	-0.628 (2.26)	3.572 (1.80)	0.493 (0.38)
	5th	0.1	-1.135 (3.60)	6.412 (2.92)	0.627 (0.87)
	7th	0.13	-1.475 (4.93)	9.210 (4.10)	0.523 (1.63)
	9th	0.17	-1.982 (6.02)	11.708 (5.09)	0.385 (2.53)
Intima	3rd	0.06	-0.370 (2.93)	4.134 (2.01)	-2.470 (10.00)
	5th	0.1	-0.717 (4.68)	7.579 (3.22)	-3.383 (14.95)
	7th	0.13	-1.105 (6.36)	10.846 (4.38)	-4.156 (18.03)
	9th	0.17	-1.688 (8.12)	13.758 (5.22)	-5.080 (19.37)
Media	3rd	0.06	-0.733 (2.55)	3.658 (1.88)	0.645 (1.60)
	5th	0.1	-1.309 (3.94)	6.555 (2.96)	0.919 (1.50)
	7th	0.13	-1.726 (5.18)	9.555 (3.94)	1.152 (1.22)
	9th	0.17	-2.225 (6.19)	12.021 (5.15)	1.627 (1.19)
Adventitia	3rd	0.06	-1.233 (2.91)	1.912 (1.63)	-2.372 (5.29)
	5th	0.1	-1.511 (4.12)	3.393 (2.70)	-3.950 (7.58)
	7th	0.13	-1.775 (4.62)	4.830 (4.07)	-4.421 (8.65)
	9th	0.17	-2.076 (5.25)	5.926 (5.35)	-4.922 (11.71)

Table 11: The average Green-Lagrange strains from the experiment for Aorta3

Type	Loading step	Measured stress(MPa)	E_{xx} (%) (std)	E_{yy} (%) (std)	E_{zz} (%) (std)
Global	3rd	0.08	-1.315 (1.28)	4.940 (0.62)	-0.269 (0.71)
	5th	0.12	-2.303 (1.92)	8.377 (1.03)	-0.708 (1.66)
	7th	0.17	-2.923 (2.54)	11.174 (1.24)	-1.020 (2.76)
	9th	0.21	-3.368 (3.08)	14.004 (1.60)	-1.124 (3.80)
Intima	3rd	0.08	-1.506 (1.13)	4.929 (0.58)	-1.655 (3.22)
	5th	0.12	-2.642 (1.82)	8.405 (0.89)	-3.531 (5.50)
	7th	0.17	-3.432 (2.45)	11.206 (1.02)	-5.844 (8.40)
	9th	0.21	-3.978 (2.94)	14.030 (1.34)	-7.480 (10.18)
Media	3rd	0.08	-1.235 (1.55)	4.909 (0.69)	0.156 (0.71)
	5th	0.12	-2.210 (2.17)	8.342 (1.06)	0.279 (0.70)
	7th	0.17	-2.836 (2.88)	11.166 (1.26)	0.687 (1.08)
	9th	0.21	-3.287 (3.36)	14.069 (1.57)	1.472 (1.40)
Adventitia	3rd	0.08	-1.367 (1.47)	4.860 (1.01)	-2.878 (4.84)
	5th	0.12	-2.213 (2.13)	8.097 (1.66)	-5.542 (7.43)
	7th	0.17	-2.590 (2.60)	10.910 (2.24)	-8.711 (11.56)
	9th	0.21	-3.072 (3.25)	13.703 (2.71)	-11.764 (13.49)

Table 12: The identification results for experimental measurements from different initial guesses

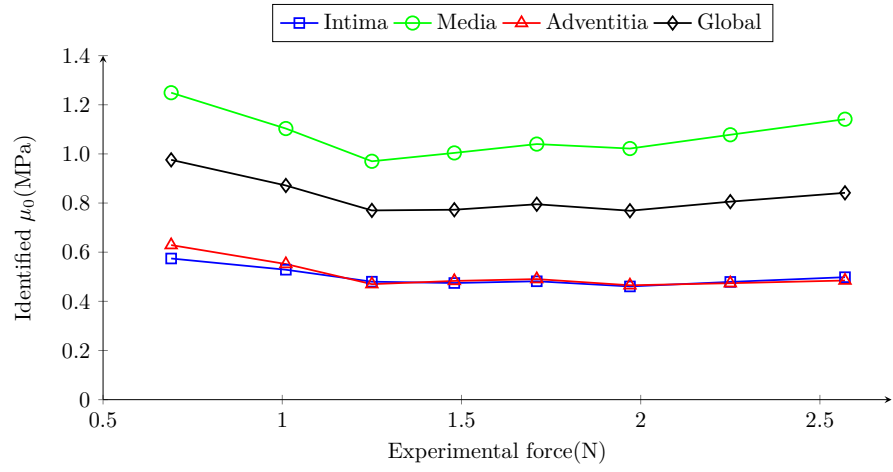
Initial guesses μ (MPa)				Identified values $\tilde{\mu}$ (MPa)		
Intima	Media	Adventitia	-	Intima	Media	Adventitia
0.1	0.1	0.1	-	0.4746	1.0040	0.4831
0.2	0.2	0.2	-	0.4746	1.0040	0.4831
0.3	0.3	0.3	-	0.4746	1.0040	0.4831
0.4	0.4	0.4	-	0.4746	1.0040	0.4831
1.0	1.0	1.0	-	0.4746	1.0040	0.4831
2.0	2.0	2.0	-	0.4746	1.0040	0.4831
3.0	3.0	3.0	-	0.4746	1.0040	0.4831
10.0	10.0	10.0	-	0.4746	1.0040	0.4831
1.0	2.0	3.0	-	0.4746	1.0040	0.4831
3.0	2.0	1.0	-	0.4746	1.0040	0.4831

352 Firstly, we investigate the influence of initial guess on the identification results as shown
353 in Table 12, in which one group of experimental measurements in Table 9 is used, it is shown
354 that the identified results for different layers of arteries are the same for ten different group of
355 initial guesses. Then, the identification results for three samples using the proposed VFM are
356 shown in Figs. 11(a), 11(b), and 11(c), respectively. Despite the chemoelastic effects going
357 on in these samples, the identified shear moduli show only marginal variations with the
358 applied force, indicating that the identification method is able to eliminate the non-purely
359 elastic effects. Indeed, it is assumed that these effects only affect the hydrostatic pressure
360 to which the VFM is immune. This assumption permitted the separate identification of the
361 shear modulus of each layer, as shown in Fig. 12. The largest shear moduli are obtained in
362 the media layer, with values of approximately 1 MPa. The intima and adventitia appeared
363 to be at least half as stiff. Although the obtained absolute values may be specific to the
364 conditions used for the purpose of this study (immersion in PG to induce osmotic effects),
365 the relative values between each layer indicate a significant gradient of elastic properties
366 across the thickness.

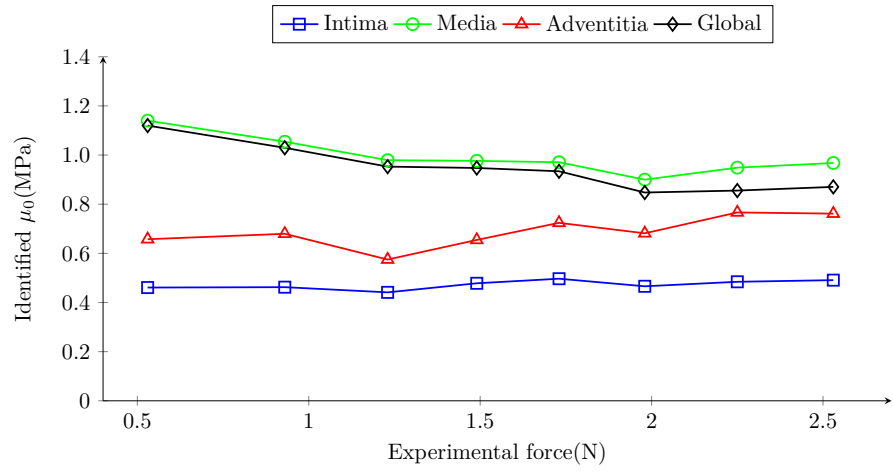
367 4. Conclusion and discussion

368 The mechanical behavior of soft biological tissues can be significantly affected by the
369 chemical potentials of interstitial fluids, resulting in obvious chemomechanical coupling phe-
370 nomena. And chemoelastic constitutive models are widely used for soft biological tissues.
371 However, to the best of our knowledge, there have been very few studies related to param-
372 eter identification of these models using VFM combined with optical full-field measurement
373 techniques.

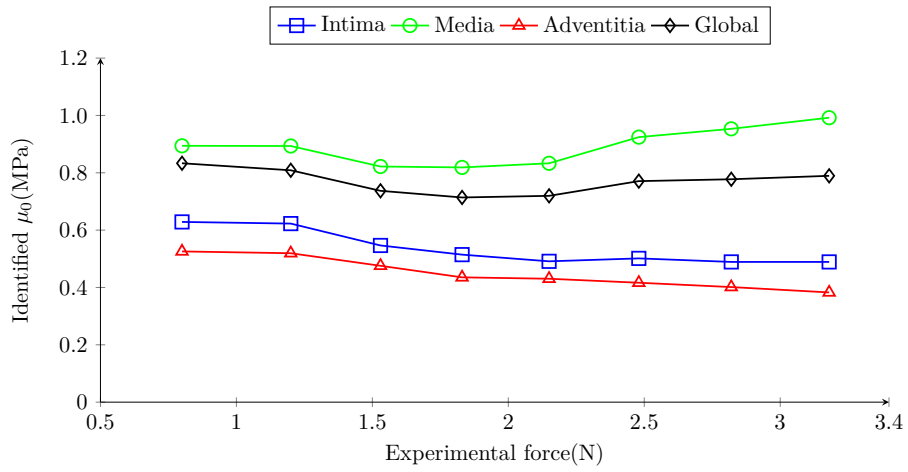
374 In this paper, VFM was applied for the parameter identification of biphasic chemoelastic
375 models using full-field measurements. The proposed approach avoids iterative resolutions



(a)



(b)



(c)

Figure 11: Identified shear moduli of tested samples with average strains across each layer and the entire aortic wall. (a) Aorta1, (b)Aorta2,(c)Aorta3.

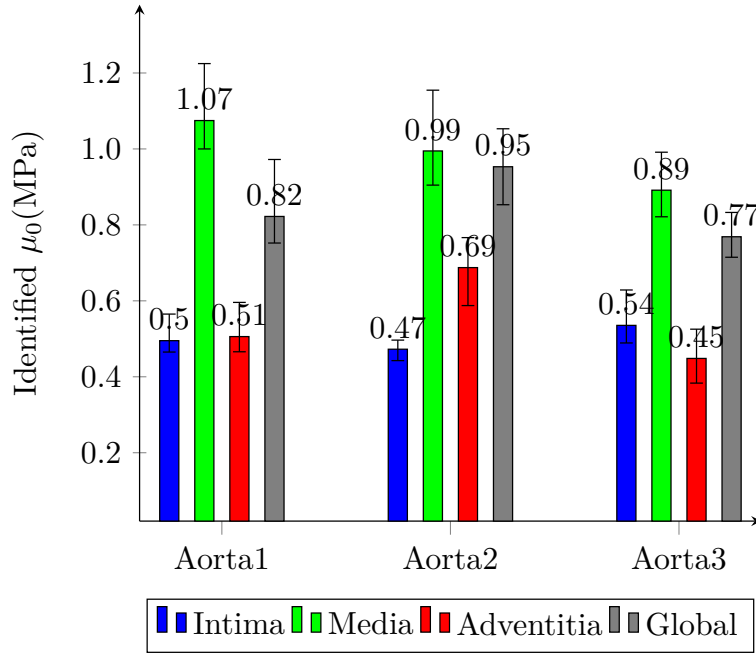


Figure 12: Identified shear moduli (mean value and deviation bar) for each layer of the tested samples

376 of direct problems with complex nonlinear chemomechanical interaction relationships. An
 377 advantage of the proposed approach is that it can extract hyperelastic parameters without
 378 knowing the chemoelastic parameters of the model simply by designing a special virtual field.
 379 Therefore, the proposed approach will be useful for further parameter identifications in soft
 380 biological tissues.

381 The proposed approach was assessed to identify the layer-specific stiffness properties of
 382 arteries based on strain fields. The identification results based on numerical simulations
 383 showed that the proposed model is immune to chemoelastic effects. Moreover, the shear
 384 modulus of the media of porcine descending thoracic aortas immersed in an 80% PG so-
 385 lution was identified with values of approximately 1 MPa, however, the identified shear
 386 modulus is smaller than the instantaneous shear modulus, which was identified to be ap-
 387 proximately 3 MPa in a previous work^[17]. Indeed, the instantaneous shear modulus was
 388 found by assuming incompressibility of the solid part in the biphasic hyperelastic model,
 389 whereas identification with the VFM did not require such an assumption. Another interest-
 390 ing finding is that the layer-specific shear moduli can be identified simultaneously with the
 391 VFM. The shear modulus of the media layer is nearly twice as stiff as that of the intima and
 392 adventitia. The ratios between interlayer shear moduli of arteries are similar to those ob-
 393 tained in the work of Peña et al.^[43], in which they were approximately 1:2:1. Therefore, the
 394 proposed approach was proved to provide an effective identification of interlayer gradients of
 395 shear moduli despite the chemoelastic effects. A potential application of the proposed VFM
 396 approach is the multiscale mechanical characterization of biological tissues since both the
 397 effective material parameters at the macroscopic scale (as in Example 1) and the multilayer

398 or heterogeneous material parameters at the mesoscopic scale (as in Examples 2 and 3) can
399 be well identified, showing effective multiscale identification for soft biological tissues even
400 in the presence of chemoelastic effects.

401 A main limitation in this study is that the VFM was only tested with the neo-Hookean
402 model. Due to the obvious anisotropic behavior of aortic wall, future work will extend
403 the approach to anisotropic hyperelastic models, such as the Holzapfel^[44] and MA-HGO^[45]
404 models which are used extensively to model collagen fibre reinforced biological materials,
405 and the use of neo-Hookean model could produce a systematic variation of the apparent
406 shear modulus with increasing strain. Another limitation of the work is that we ignore the
407 stiffening effect of soft tissues for the sake of simplicity, a more complex VFM for nonlinear
408 problems is required to consider this case.

409 In summary, we have presented a new VFM approach for parameter identification that
410 is well suited for chemoelastic constitutive relationships in soft biological tissues. The iden-
411 tification of layer-specific elastic parameters can be applied even in the presence of complex
412 chemoelastic effects. Important developments will extend the approach to multiscale consti-
413 tutive models, and anisotropic effects of soft tissues.

414 **Declaration of competing interest**

415 The authors declare that they have no known competing financial interests or personal
416 relationships that could have appeared to influence the work reported in this paper.

417 **Acknowledgements**

418 The research leading to this paper was funded by the NSFC Grants [12072063, 11972109],
419 the Fundamental Research Funds for the Central Universities [DUT21YG129], the Grants of
420 State Key Laboratory of Structural Analysis for Industrial Equipment [S22403, GZ21104],
421 and the Alexander von Humboldt Foundation [1217594].

422 **Data availability statement**

423 The data discussed in this work are available on request.

424 **References**

- 425 [1] Y. Lanir, Osmotic swelling and residual stress in cardiovascular tissues, *Journal of*
426 *Biomechanics* 45 (2012) 780–789. doi:[10.1016/j.jbiomech.2011.11.018](https://doi.org/10.1016/j.jbiomech.2011.11.018).
- 427 [2] A. E. Ehret, K. Bircher, A. Stracuzzi, V. Marina, M. Zündel, E. Mazza, Inverse poroe-
428 lasticity as a fundamental mechanism in biomechanics and mechanobiology, *Nature*
429 *Communications* 8 (2017) 1002. doi:[10.1038/s41467-017-00801-3](https://doi.org/10.1038/s41467-017-00801-3).

- 430 [3] I. S. Kovach, The importance of polysaccharide configurational entropy in determin-
431 ing the osmotic swelling pressure of concentrated proteoglycan solution and the bulk
432 compressive modulus of articular cartilage, *Biophysical Chemistry* 53 (1995) 181–187.
433 doi:[10.1016/0301-4622\(94\)00100-X](https://doi.org/10.1016/0301-4622(94)00100-X).
- 434 [4] Y. Lanir, Biorheology and fluid flux in swelling tissues. I. Bicomponent theory for
435 small deformations, including concentration effects, *Biorheology* 24 (1987) 173–187.
436 doi:[10.3233/BIR-1987-24210](https://doi.org/10.3233/BIR-1987-24210).
- 437 [5] A. Eringen, J. D. Ingram, A continuum theory of chemically reacting media—I, *Inter-*
438 *national Journal of Engineering Science* 3 (1965) 197–212. doi:[10.1016/0020-7225\(65\)](https://doi.org/10.1016/0020-7225(65)90044-3)
439 [90044-3](https://doi.org/10.1016/0020-7225(65)90044-3).
- 440 [6] J. D. Ingram, A. Eringen, A continuum theory of chemically reacting media—II Consti-
441 tutive equations of reacting fluid mixtures, *International Journal of Engineering Science*
442 5 (1967) 289–322. doi:[10.1016/0020-7225\(67\)90040-7](https://doi.org/10.1016/0020-7225(67)90040-7).
- 443 [7] V. C. Mow, S. C. Kuei, W. M. Lai, C. G. Armstrong, Biphasic creep and stress relaxation
444 of articular cartilage in compression: theory and experiments, *Journal of Biomechanical*
445 *Engineering* 102 (1980) 73–84. doi:[10.1115/1.3138202](https://doi.org/10.1115/1.3138202).
- 446 [8] W. M. Lai, J. S. Hou, V. C. Mow, A triphasic theory for the swelling and deformation
447 behaviors of articular cartilage, *Journal of Biomechanical Engineering* 113 (1991) 245–
448 258. doi:[10.1115/1.2894880](https://doi.org/10.1115/1.2894880).
- 449 [9] G. A. Ateshian, N. O. Chahine, I. M. Basalo, C. T. Hung, The correspondence between
450 equilibrium biphasic and triphasic material properties in mixture models of articular
451 cartilage, *Journal of Biomechanics* 37 (2004) 391–400. doi:[10.1016/S0021-9290\(03\)](https://doi.org/10.1016/S0021-9290(03)00252-5)
452 [00252-5](https://doi.org/10.1016/S0021-9290(03)00252-5).
- 453 [10] G. A. Ateshian, B. J. Ellis, J. A. Weiss, Equivalence between short-time biphasic and
454 incompressible elastic material responses, *Journal of Biomechanical Engineering* 129
455 (2007) 405–412. doi:[10.1115/1.2720918](https://doi.org/10.1115/1.2720918).
- 456 [11] G. A. Ateshian, V. Rajan, N. O. Chahine, C. E. Canal, C. T. Hung, Modeling the
457 matrix of articular cartilage using a continuous fiber angular distribution predicts many
458 observed phenomena, *Journal of Biomechanical Engineering* 131 (2009) 061003. doi:[10.](https://doi.org/10.1115/1.3118773)
459 [1115/1.3118773](https://doi.org/10.1115/1.3118773).
- 460 [12] W. Wilson, C. C. van Donkelaar, J. M. Huyghe, A comparison between mechano-
461 electrochemical and biphasic swelling theories for soft hydrated tissues, *Journal of*
462 *Biomechanical Engineering* 127 (2005) 158–165. doi:[10.1115/1.1835361](https://doi.org/10.1115/1.1835361).
- 463 [13] J. S. Wayne, S. L.-Y. Woo, M. K. Kwan, Application of the u-p finite element method
464 to the study of articular cartilage, *Journal of Biomechanical Engineering* 113 (1991)
465 397–403. doi:[10.1115/1.2895418](https://doi.org/10.1115/1.2895418).

- 466 [14] K. Kandil, F. Zaïri, A. Derrouiche, T. Messenger, F. Zaïri, Interlamellar-induced time-
467 dependent response of intervertebral disc annulus: A microstructure-based chemo-
468 viscoelastic model, *Acta Biomaterialia* 100 (2019) 75–91. doi:[10.1016/j.actbio.2019.](https://doi.org/10.1016/j.actbio.2019.10.005)
469 [10.005](https://doi.org/10.1016/j.actbio.2019.10.005).
- 470 [15] E. U. Azeloglu, M. B. Albro, V. A. Thimmappa, G. A. Ateshian, K. D. Costa, Het-
471 erogeneous transmural proteoglycan distribution provides a mechanism for regulating
472 residual stresses in the aorta, *American Journal of Physiology-Heart and Circulatory*
473 *Physiology* 294 (2008) H1197–H1205. doi:[10.1152/ajpheart.01027.2007](https://doi.org/10.1152/ajpheart.01027.2007).
- 474 [16] V. A. Acosta Santamaría, M. F. García, J. Molimard, S. Avril, Three-dimensional
475 full-field strain measurements across a whole porcine aorta subjected to tensile loading
476 using optical coherence tomography–digital volume correlation, *Frontiers in Mechanical*
477 *Engineering* 4 (2018) 3. doi:[10.3389/fmech.2018.00003](https://doi.org/10.3389/fmech.2018.00003).
- 478 [17] V. A. Acosta Santamaría, M. F. García, J. Molimard, S. Avril, Characterization of
479 chemoelastic effects in arteries using digital volume correlation and optical coherence
480 tomography, *Acta Biomaterialia* 102 (2020) 127–137. doi:[10.1016/j.actbio.2019.11.](https://doi.org/10.1016/j.actbio.2019.11.049)
481 [049](https://doi.org/10.1016/j.actbio.2019.11.049).
- 482 [18] S. Avril, S. Evans (Eds.), *Material Parameter Identification and Inverse Problems in Soft*
483 *Tissue Biomechanics*, volume 573 of *CISM International Centre for Mechanical Sciences*,
484 Springer International Publishing, Cham, 2017. doi:[10.1007/978-3-319-45071-1](https://doi.org/10.1007/978-3-319-45071-1).
- 485 [19] S. Avril, M. Bonnet, A.-S. Bretelle, M. Grédiac, F. Hild, P. Ienny, F. Latourte,
486 D. Lemosse, S. Pagano, E. Pagnacco, F. Pierron, Overview of identification methods of
487 mechanical parameters based on full-field measurements, *Experimental Mechanics* 48
488 (2008) 381–402. doi:[10.1007/s11340-008-9148-y](https://doi.org/10.1007/s11340-008-9148-y).
- 489 [20] F. Pierron, M. Grédiac, *The Virtual Fields Method*, Springer New York, New York,
490 NY, 2012. doi:[10.1007/978-1-4614-1824-5](https://doi.org/10.1007/978-1-4614-1824-5).
- 491 [21] M. Grédiac, Principe des travaux virtuels et identification. (Principle of virtual work
492 and identification), *Comptes Rendus de l’Académie des Sciences. Série II* 309 (1989).
- 493 [22] M. Grédiac, E. Toussaint, F. Pierron, Special virtual fields for the direct deter-
494 mination of material parameters with the virtual fields method. 1—Principle and
495 definition, *International Journal of Solids and Structures* 39 (2002) 2691–2705.
496 doi:[10.1016/S0020-7683\(02\)00127-0](https://doi.org/10.1016/S0020-7683(02)00127-0).
- 497 [23] M. Grédiac, E. Toussaint, F. Pierron, Special virtual fields for the direct determi-
498 nation of material parameters with the virtual fields method. 2—Application to in-
499 plane properties, *International Journal of Solids and Structures* 39 (2002) 2707–2730.
500 doi:[10.1016/S0020-7683\(02\)00128-2](https://doi.org/10.1016/S0020-7683(02)00128-2).

- 501 [24] M. Grédiac, E. Toussaint, F. Pierron, Special virtual fields for the direct determination
502 of material parameters with the virtual fields method. 3. Application to the bending
503 rigidities of anisotropic plates, *International Journal of Solids and Structures* 40 (2003)
504 2401–2419. doi:[10.1016/S0020-7683\(03\)00030-1](https://doi.org/10.1016/S0020-7683(03)00030-1).
- 505 [25] Y. Mei, J. Liu, X. Guo, B. Zimmerman, T. D. Nguyen, S. Avril, General finite-element
506 framework of the virtual fields method in nonlinear elasticity, *Journal of Elasticity*
507 (2021). doi:[10.1007/s10659-021-09842-8](https://doi.org/10.1007/s10659-021-09842-8).
- 508 [26] Y. Mei, J. Deng, X. Guo, S. Goenezen, S. Avril, Introducing regularization into the
509 virtual fields method (VFM) to identify nonhomogeneous elastic property distributions,
510 *Computational Mechanics* 67 (2021) 1581–1599. doi:[10.1007/s00466-021-02007-3](https://doi.org/10.1007/s00466-021-02007-3).
- 511 [27] M. Grédiac, F. Pierron, S. Avril, E. Toussaint, The virtual fields method for extracting
512 constitutive parameters from full-field measurements: a review, *Strain* 42 (2008) 233–
513 253. doi:[10.1111/j.1475-1305.2006.tb01504.x](https://doi.org/10.1111/j.1475-1305.2006.tb01504.x).
- 514 [28] S. Avril, M. Grédiac, F. Pierron, Sensitivity of the virtual fields method to noisy data,
515 *Computational Mechanics* 34 (2004) 439–452. doi:[10.1007/s00466-004-0589-6](https://doi.org/10.1007/s00466-004-0589-6).
- 516 [29] S. Avril, F. Pierron, General framework for the identification of constitutive parameters
517 from full-field measurements in linear elasticity, *International Journal of Solids and*
518 *Structures* 44 (2007) 4978–5002. doi:[10.1016/j.ijsolstr.2006.12.018](https://doi.org/10.1016/j.ijsolstr.2006.12.018).
- 519 [30] S. Avril, P. Badel, A. Duprey, Anisotropic and hyperelastic identification of in vitro
520 human arteries from full-field optical measurements, *Journal of Biomechanics* 43 (2010)
521 2978–2985. doi:[10.1016/j.jbiomech.2010.07.004](https://doi.org/10.1016/j.jbiomech.2010.07.004).
- 522 [31] J.-H. Kim, S. Avril, A. Duprey, J.-P. Favre, Experimental characterization of rupture
523 in human aortic aneurysms using a full-field measurement technique, *Biomechanics and*
524 *Modeling in Mechanobiology* 11 (2012) 841–853. doi:[10.1007/s10237-011-0356-5](https://doi.org/10.1007/s10237-011-0356-5).
- 525 [32] M. R. Bersi, C. Bellini, P. Di Achille, J. D. Humphrey, K. Genovese, S. Avril, Novel
526 methodology for characterizing regional variations in the material properties of murine
527 aortas, *Journal of Biomechanical Engineering* 138 (2016) 071005. doi:[10.1115/1.](https://doi.org/10.1115/1.4033674)
528 [4033674](https://doi.org/10.1115/1.4033674).
- 529 [33] N. O. Chahine, F. H. Chen, C. T. Hung, G. A. Ateshian, Direct measurement of osmotic
530 pressure of glycosaminoglycan solutions by membrane osmometry at room temperature,
531 *Biophysical Journal* 89 (2005) 1543–1550. doi:[10.1529/biophysj.104.057315](https://doi.org/10.1529/biophysj.104.057315).
- 532 [34] F. G. Donnan, The theory of membrane equilibria., *Chemical Reviews* 1 (1924) 73–90.
533 doi:[10.1021/cr60001a003](https://doi.org/10.1021/cr60001a003).
- 534 [35] J. Overbeek, The donnan equilibrium, *Progress in Biophysics and Biophysical Chem-*
535 *istry* 6 (1956) 57–84. doi:[10.1016/S0096-4174\(18\)30104-5](https://doi.org/10.1016/S0096-4174(18)30104-5).

- 536 [36] A. F. Bower, *Applied Mechanics of Solids*, CRC Press, 2009. doi:[10.1201/
537 9781439802489](https://doi.org/10.1201/9781439802489).
- 538 [37] Y. Mei, S. Avril, On improving the accuracy of nonhomogeneous shear modulus identifi-
539 cation in incompressible elasticity using the virtual fields method, *International Journal
540 of Solids and Structures* 178-179 (2019) 136–144. doi:[10.1016/j.ijsolstr.2019.06.
541 025](https://doi.org/10.1016/j.ijsolstr.2019.06.025).
- 542 [38] J. C. Lagarias, J. A. Reeds, M. H. Wright, P. E. Wright, Convergence Properties of the
543 Nelder–Mead Simplex Method in Low Dimensions, *SIAM Journal on Optimization* 9
544 (1998) 112–147. doi:[10.1137/S1052623496303470](https://doi.org/10.1137/S1052623496303470).
- 545 [39] P. Thakolkaran, A. Joshi, Y. Zheng, M. Flaschel, L. De Lorenzis, S. Kumar, NN-
546 EUCLID: Deep-learning hyperelasticity without stress data, *Journal of the Mechanics
547 and Physics of Solids* 169 (2022) 105076. doi:[10.1016/j.jmps.2022.105076](https://doi.org/10.1016/j.jmps.2022.105076).
- 548 [40] M. Flaschel, S. Kumar, L. De Lorenzis, Unsupervised discovery of interpretable hypere-
549 lastic constitutive laws, *Computer Methods in Applied Mechanics and Engineering* 381
550 (2021) 113852. doi:[10.1016/j.cma.2021.113852](https://doi.org/10.1016/j.cma.2021.113852).
- 551 [41] H. Yiqian, Y. Haitian, Solving inverse couple-stress problems via an element-free
552 Galerkin (EFG) method and Gauss–Newton algorithm, *Finite Elements in Analysis
553 and Design* 46 (2010) 257–264. doi:[10.1016/j.finel.2009.09.009](https://doi.org/10.1016/j.finel.2009.09.009).
- 554 [42] T. Waffenschmidt, C. Polindara, A. Menzel, S. Blanco, A gradient-enhanced large-
555 deformation continuum damage model for fibre-reinforced materials, *Computer Methods
556 in Applied Mechanics and Engineering* 268 (2014) 801–842. doi:[10.1016/j.cma.2013.
557 10.013](https://doi.org/10.1016/j.cma.2013.10.013).
- 558 [43] J. A. Peña, M. A. Martínez, E. Peña, Layer-specific residual deformations and uniaxial
559 and biaxial mechanical properties of thoracic porcine aorta, *Journal of the Mechanical
560 Behavior of Biomedical Materials* 50 (2015) 55–69. doi:[10.1016/j.jmbbm.2015.05.024](https://doi.org/10.1016/j.jmbbm.2015.05.024).
- 561 [44] G. A. Holzapfel, T. C. Gasser, R. W. Ogden, A new constitutive framework for arterial
562 wall mechanics and a comparative study of material models, in: S. C. Cowin, J. D.
563 Humphrey (Eds.), *Cardiovascular Soft Tissue Mechanics*, Kluwer Academic Publishers,
564 Dordrecht, 2004, pp. 1–48. doi:[10.1007/0-306-48389-0_1](https://doi.org/10.1007/0-306-48389-0_1).
- 565 [45] D. Nolan, A. Gower, M. Destrade, R. Ogden, J. McGarry, A robust anisotropic hyper-
566 elastic formulation for the modelling of soft tissue, *Journal of the Mechanical Behavior
567 of Biomedical Materials* 39 (2014) 48–60. doi:[10.1016/j.jmbbm.2014.06.016](https://doi.org/10.1016/j.jmbbm.2014.06.016).